

# Efficient broadband THz generation in BNA organic crystal at Ytterbium laser wavelength

HOVAN LEE,<sup>1,\*</sup> CLAUDIA GOLLNER,<sup>2</sup> JIAQI NIE,<sup>4,</sup> YAN ZHANG,<sup>4</sup>  
CEDRIC WEBER,<sup>1</sup> AND MOSTAFA SHALABY<sup>3,4,†</sup>

<sup>1</sup>*Department of Physics, Faculty of Natural & Mathematical Sciences, King's College London, London, WC2R2LS, UK*

<sup>2</sup>*Photonics Institute, TU Wien, Gusshausstrasse 27-387, A-1040 Vienna, Austria*

<sup>3</sup>*Swiss Terahertz Research-Zurich, Techpark, 8005 Zurich, Switzerland and Park Innovaare, 5234 Villigen, Switzerland*

<sup>4</sup>*Key Laboratory of Terahertz Optoelectronics, Beijing Advanced Innovation Center for Imaging Technology Capital Normal University, Beijing 100048, China*

\**hovan.lee@kcl.ac.uk*

†*most.shalaby@gmail.com*

**Abstract:** In this work, we demonstrate BNA's high potential for efficient generation of high power THz using ytterbium laser wavelengths. We study the generation theoretically and experimentally using laser wavelength of 960 – 1150 nm. Broadband pulses of 0 – 7 THz and high efficiency of 0.6% are demonstrated.

© 2021 Optical Society of America under the terms of the [OSA Open Access Publishing Agreement](#)

## 1. Introduction

Throughout the past decades, THz technology (0.1 – 10 THz) have proven invaluable in numerous disciplines [1–3] ranging from ultrafast magnetisation [4–7] to biomedical sciences [8–11], amongst others [12–17]. However, one major hurdle exists across all THz applications: The lack of convenience in generating THz radiation.

Regarding this problem, optical rectification (OR) of nonlinear crystals offers a suitable solution, as this method offers the portability and ease-of-use as a tabletop THz source, whilst maintaining a large optical to THz conversion efficiency. One advantage of this method comes from the freedom of choice in crystals, where the applicable pump wavelength range and THz spectrum can be changed according to the requirements of the situation.

In OR, the nonlinear crystal is pumped with a femtosecond (fs) electromagnetic pulse, and a frequency dependant polarisation is induced within the crystal. Due the wide spectral contents of the fs pulse, the different frequency components superpose in the form of a beating polarisation, leading to emissions in the THz range.

Different crystals respond to pump pulses differently, generating characteristic THz spectra. In this regard, Lithium Niobate is a popular crystal for THz generation [18–21]. However, the spectrum is mainly limited to sub 1 THz and the generation geometry is complex (non collinear) to achieve phase matching.

In this sense, DAST [22, 23] and its derivative DSTMS [24], have been shown to generate wide THz spectra up towards 20 THz, with favourable phase matching conditions when paired with a pump pulse of wavelength  $\sim 1.5 \mu\text{m}$ . This presents another problem, as the availability of conventional lasers at this spectral range is limited; most groups rely upon Optical Parametric Amplifiers (OPAs) in order to convert Ti:Sa (800 nm) or Yb (1030 nm) lasers to longer wavelengths.

Conversely, BNA (N-benzyl-2-methyl-4-nitroaniline) features phase matching at optical wavelengths below 1200 nm, alleviating the shortcomings of DAST. In support of this claim, past reports on BNA demonstrated 0.2 – 3 THz spectra at 0.2% conversion efficiency and 0.2 – 7

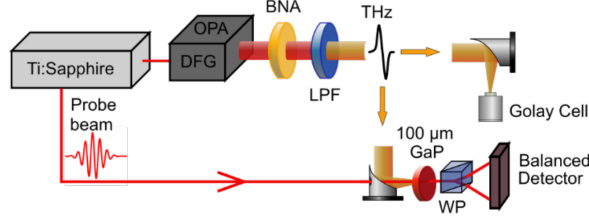


Fig. 1. Schematic diagram of the experimental setup.

THz spectra at 0.8% efficiency when pumped with 800 nm Ti:Sa [25] and 1200 – 1120 nm near infrared [26] respectively.

In this work, we demonstrate BNA's high potential of THz generation by providing experimental data and theoretical analysis of the spectra generated under the more and more conventional ytterbium laser wavelengths of 960 – 1150 nm with varied crystal thicknesses.

## 2. Method

### 2.1. Experimental Setup

The ytterbium laser was not available to us. Therefore, to achieve the specified pump wavelengths, we used a setup with similar wavelengths and higher tunability based on a 1kHz OPA equipped with a difference frequency generation (DFG) unit, pumped by a 3.5 mJ, 800 nm, 35 fs laser. The OPA beam is then sent to the BNA crystal (with variable thicknesses of 300 μm, 550 μm, 1100 μm, from SwissTHz) through which the THz spectra are collinearly generated. The THz spectra are then refined through three low pass filters (LPF) with out-of-band rejection ratio of > 0.1% to filter out the residual NIR frequencies. Subsequently the filtered THz spectra are expanded and focused with a set of three off axis mirrors, and detected with either a Golay cell (MTI Inc.), an electro-optical sampler (100 μm GaP, from SwizzTHz), or a RIGI uncooled mircobolometer camera (from SwissTHz).

### 2.2. Theoretical Spectra Calculation

The simulated THz spectra and phase matching conditions were calculated by following the OR framework of Schneider Et Al. [27]; through considering the solution to the nonlinear wave equation inside BNA crystals:

$$-\nabla \times \nabla \times \mathbf{E}(\mathbf{r}, \omega) + \omega^2 \mu_0 \epsilon_0 \epsilon(\omega) \otimes \mathbf{E}(\mathbf{r}, \omega) - i\omega \mu_0 \sigma(\omega) \otimes \mathbf{E}(\mathbf{r}, \omega) = -\omega^2 \mu_0 \mathbf{P}_{NL}(\mathbf{r}, \omega) \quad (1)$$

Where  $\mathbf{E}$  is the electric field,  $\epsilon$  is the dielectric tensor,  $\sigma$  is the optical conductivity tensor, and  $\mathbf{P}_{NL}$  is the nonlinear polarisation (and can be expanded in powers of  $\mathbf{E}$ ), all evaluated at frequency  $\omega$  and position  $\mathbf{r}$ . Taking only the quadratic term in  $\mathbf{P}_{NL}$ :

$$P_{NL,i}(\omega) = \epsilon_0 \int d\omega' \chi_{ijk}^{(2)}(\omega; \omega', \omega - \omega') E_j(\omega') E_k(\omega - \omega') \quad (2)$$

With  $P_{NL,i}$  as the nonlinear polarisation in the  $i$  direction, and  $\chi_{ijk}^{(2)}$  is the 2nd order susceptibility of the material. The Electric field of the laser pulse may be characterised as a single axis polarised, time varying, complex amplitude  $E_{0,k}(t)$  propagating with carrier frequency  $\omega_0$ . This simplifies the nonlinear response by decreasing the number of active elements of the susceptibility tensor to  $\chi_{ikk}^{(2)}$ . This susceptibility can be further simplified if  $\omega_0$  is far away from

any resonance frequency of the material, and only OR effects are considered in  $P_{NL}$ , leaving the susceptibility  $\chi^{OR}(\omega; \omega_0)$  as a function of only  $\omega_0$  and the resultant THz polarisation frequency  $\omega$ .

Implementing these adjustments to the nonlinear wave equation and solving for the electric field gives:

$$E(\omega, z) = \frac{\mu_0 \chi^{OR}(\omega; \omega_0) \omega I_0(\omega)}{n(\omega_0) \left\{ \frac{c}{\omega} \left[ \frac{\alpha_T(\omega)}{2} + \alpha_0 \right] + i[n(\omega) + n_g] \right\}} \frac{\exp[-i \frac{\omega n(\omega)}{c} z] \exp[-\frac{\alpha_T(\omega)}{2} z] - \exp(-i \frac{\omega n_g}{c} z) \exp(-\alpha_0 z)}{\frac{\alpha_T(\omega)}{2} - \alpha_0 + i \frac{\omega}{c} [n(\omega) - n_g]} \quad (3)$$

Here,  $I_0$  is the pump pulse spectrum that has transmitted through the incident interface of the crystal,  $n(\omega)$  is the refractive index of the crystal at frequency  $\omega$ ,  $n_g$  is the group index of the pump pulse,  $\alpha_0$  and  $\alpha_T$  are the absorption coefficient of the crystal at the pump pulses and THz frequencies respectively,  $c$  is the speed of light, and lastly  $z$  is the propagation depth of the pump pulse.

The second fraction in Eq.3 is a complex entity with the unit of a length. The magnitude of this fraction is at its highest when the absorption coefficients  $\alpha_T$  and  $\alpha_0$  are low, and when the phase of the pump and the THz pulses match ( $n(\omega) = n_g$ ). Therefore, the magnitude of this fraction can be defined as the effective generation length:

$$L_{gen}(\omega, z) = \left( \frac{\exp[-\alpha_T(\omega)z] + \exp(-2\alpha_0 z) - 2 \exp\{-[\frac{\alpha_T(\omega)}{2} + \alpha_0]z\} \cos\{\frac{\omega}{c} [n(\omega) - n_g]z\}}{[\frac{\alpha_T(\omega)}{2} - \alpha_0]^2 + (\frac{\omega}{c})^2 [n(\omega) - n_g]^2} \right)^{1/2} \quad (4)$$

The various electromagnetic attributes of BNA, as was utilised in these calculations are as follows: refractive index in the THz range was obtained through Lorentz oscillator fitting of the experimental data, THz range absorption from the Lorentz oscillator parameters of Miyamoto Et Al. [28], optical range refractive index from the Sellmeier equation parameters presented in [29], the optical range absorption was calculated from the power propagation model [30]. Lastly, the pump pulse was simulated as a Gaussian distribution in frequency through matching the FWHM of the experimental pump pulse with the standard deviation of the distribution.

### 3. Results

To demonstrate the optical to THz conversion capabilities of BNA, the THz frequency integrated amplitude of the generated spectra are presented in Fig.2.a. For a crystal of thickness  $550 \mu\text{m}$  under constant pump energy, a gradual decay of efficiency is observed as pump wavelength increases. Furthermore, Fig.2.b shows a linearly increasing trend in efficiency as pump energy density increases, with the pump wavelength tuned to  $960 \text{ nm}$ ,  $1050 \text{ nm}$ ,  $1150 \text{ nm}$ . The highest efficiency was observed at 0.6% for the measurement of the shortest pump wavelength of  $960 \text{ nm}$  and the highest pump fluence of  $1.3 \text{ mJ/cm}^2$ , without observable efficiency saturation.

Fig.3 depicts the calculated normalised coherence length of BNA. For all pump wavelengths between  $800 - 1500 \text{ nm}$  a large coherence length was observed between  $0 - 1.2 \text{ THz}$ , and decreases at higher  $\text{THz}$  frequencies with an exception of a narrow band of large length  $\sim 900 \text{ nm}$ . These results concur with those of Fig.2; THz generation efficiency is highest at  $\sim 900 \text{ nm}$ , and decreases as pump wavelength increases.

The individual normalised THz spectra, under varying pump pulse wavelengths, are presented in Fig.4 for crystal lengths of a)  $300 \mu\text{m}$ , b)  $550 \mu\text{m}$  and c)  $1100 \mu\text{m}$ . A comparison between the spectra generated with different crystal thicknesses under the pump wavelength of  $960 \text{ nm}$  is shown in Fig.4.d. These results agree with Fig.3; high spectral density were observed between  $1 - 2 \text{ THz}$  for all pump wavelengths, with a decreasing trend of spectral density at higher  $\text{THz}$  frequencies.

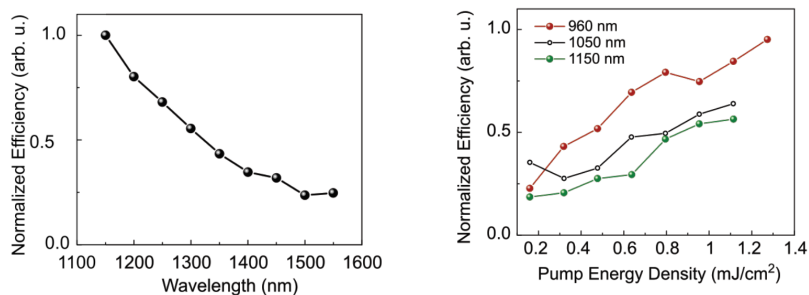


Fig. 2. Normalised optical to THz conversion efficiency as a function of a) pump wavelength and b) fluence for a  $550 \mu\text{m}$  thick BNA crystal. As pump wavelength increases, a decrease in conversion efficiency is observed in a). In b), the highest efficiencies were achieved for the shortest wavelength at  $960 \text{ nm}$ , reaching  $0.6\%$  at  $1.3 \text{ mJ/cm}^2$ . All three measurement sets suggest a linear regime; saturation of the conversion efficiency was not observed.

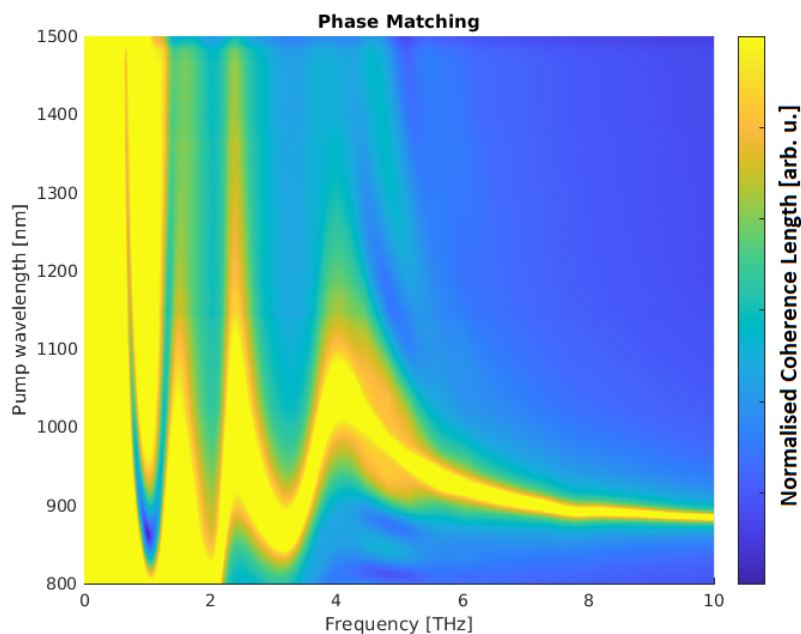


Fig. 3. Calculated normalised coherence length with respect to the pump wavelength and generated THz frequency. We observe favourable phase matching between all pump wavelengths in the range of  $0\text{-}1.2 \text{ THz}$ , with an exception of a thin band around  $1 \text{ THz}$  between the pump wavelengths of  $800\text{-}900 \text{ nm}$ . The coherence length decreases at higher THz frequencies, leaving only a thin band near the pump wavelength of  $900\text{nm}$ . The simulation confirms a broad spectrum and maximum coherence length for  $\sim 1 \mu\text{m}$  driving pulses.

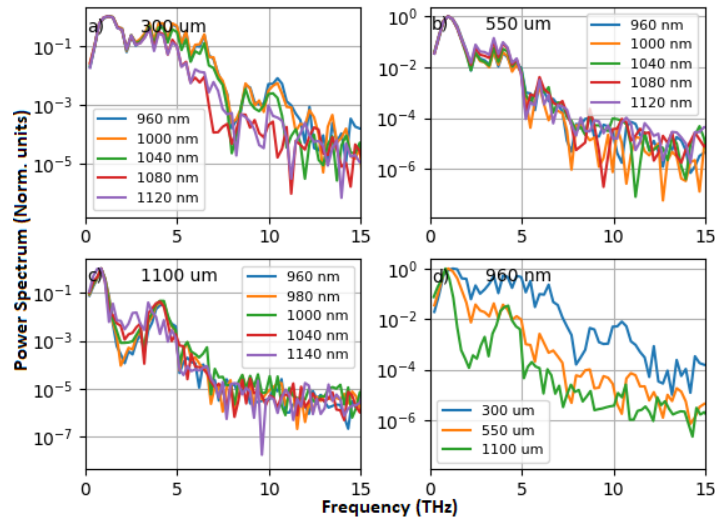


Fig. 4. Logarithmic power spectra for crystals with different thicknesses pumped with varying wavelengths. a) Crystal thickness of  $300 \mu\text{m}$ , b)  $550 \mu\text{m}$  and c)  $1100 \mu\text{m}$ . (d) Comparison of constant pump wavelength spectral contents for different crystal thicknesses.

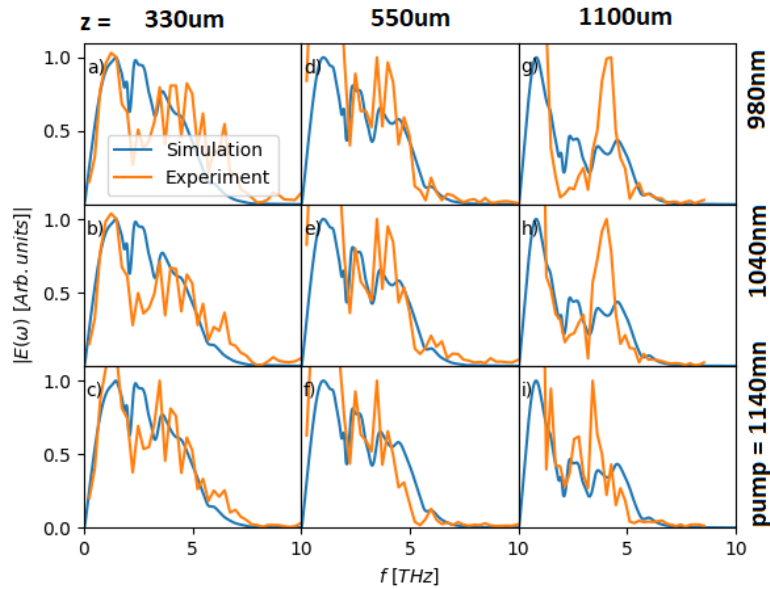


Fig. 5. Comparison between experimental (arbitrary normalisation) and simulation results for BNA crystal thickness of  $300 \mu\text{m}$  (left column),  $550 \mu\text{m}$  (middle column) and  $1100 \mu\text{m}$  (right column) at pump wavelengths of  $980 \text{ nm}$  (top row),  $1040 \text{ nm}$  (middle row),  $1140 \text{ nm}$  (bottom row).

Lastly, a comparison between the experimental data and the calculated spectra at pump wavelengths of 980, 1040 and 1140 nm is shown in Fig.5 for crystal lengths of a) 330  $\mu\text{m}$ , b) 500  $\mu\text{m}$  and c) 1100  $\mu\text{m}$ . All calculated spectra match the experimental data well at 1 – 2 THz frequencies, with an overestimate of a peak at  $\sim 2.5$  THz in the 300  $\mu\text{m}$  crystal. Moreover, a spectral peak was observed up to 4 – 5 THz in all data sets, this is in agreement with the large coherence length band at 4 THz spanning between 1000 – 1100 nm pump wavelengths. Finally, the broadest spectra (up towards 7 THz) were observed with the thinnest crystal (330  $\mu\text{m}$ ) at pump wavelengths closest to 900 nm, coinciding with the calculated coherence length.

#### 4. Conclusion

In this work, we investigate THz generation of organic crystal BNA near ytterbium laser wavelength for different crystal thicknesses and pump wavelengths. We present the THz conversion efficiency, as well as the generated spectral content, to demonstrate a linear relationship between pump energy and efficiency. The highest optical to THz conversion efficiencies, along with a broad THz spectrum reaching up to 7 THz, can be found for driving pulses centred at around 1  $\mu\text{m}$ , as demonstrated both experimentally and theoretically. This paves the way for an additional application of the Ytterbium laser wavelength, and for BNA as a potential next generation THz source.

#### 5. Disclosures

The authors declare no conflicts of interest.

#### References

1. M. Tonouchi, "Cutting-edge terahertz technology," *Nat. Photonics* **1**, 97–105 (2007).
2. P. Jepsen, D. Cooke, and M. Koch, "Terahertz spectroscopy and imaging – modern techniques and applications," *Laser & Photonics Rev.* **5**, 124–166 (2011).
3. J. B. Baxter and G. W. Guglietta, "Terahertz spectroscopy," *Anal. Chem.* **83**, 4342–4368 (2011).
4. S. Baierl, M. Hohenleutner, T. Kampfrath, A. K. Zvezdin, A. V. Kimel, R. Huber, and R. V. Mikhaylovskiy, "Nonlinear spin control by terahertz-driven anisotropy fields," *Nat. Photonics* **10**, 715 – 720 (2016).
5. M. Shalaby, C. Vicario, and C. P. Hauri, "Low frequency terahertz-induced demagnetization in ferromagnetic nickel," *Appl. Phys. Lett.* **108**, 182903 (2016).
6. D. Polley, M. Pancaldi, M. Hudl, P. Vavassori, S. Urazhdin, and S. Bonetti, "THz-driven demagnetization with perpendicular magnetic anisotropy: towards ultrafast ballistic switching," *J. Phys. D: Appl. Phys.* **51**, 084001 (2018).
7. D. J. Hilton, R. D. Averitt, C. A. Meserole, G. L. Fisher, D. J. Funk, and A. J. Taylor, "Terahertz spectroscopy of ultrafast demagnetization in ferromagnetic iron," in *2005 Quantum Electronics and Laser Science Conference*, vol. 1 (2005), pp. 347–349 Vol. 1.
8. X. Yang, X. Zhao, K. Yang, Y. Liu, Y. Liu, W. Fu, and Y. Luo, "Biomedical applications of terahertz spectroscopy and imaging," *Trends Biotechnol.* **34**, 810 – 824 (2016).
9. C. Yu, S. Fan, Y. Sun, and E. Pickwell-MacPherson, "The potential of terahertz imaging for cancer diagnosis: A review of investigations to date," *Quant. Imaging Medicine Surg.* **2** (2012).
10. Y. Sun, M. Sy, Y.-X. Wang, A. Ahuja, Y.-T. Zhang, and E. Pickwell-MacPherson, "A promising diagnostic method: Terahertz pulsed imaging and spectroscopy," *World journal radiology* **3**, 55–65 (2011).
11. Y. Wang, H. Minamide, M. Tang, T. Notake, and H. Ito, "Study of water concentration measurement in thin tissues with terahertz-wave parametric source," *Opt. Express* **18**, 15504–15512 (2010).
12. R. Ulbricht, E. Hendry, J. Shan, T. F. Heinz, and M. Bonn, "Carrier dynamics in semiconductors studied with time-resolved terahertz spectroscopy," *Rev. Mod. Phys.* **83**, 543–586 (2011).
13. L. Razzari, F. H. Su, G. Sharma, F. Blanchard, A. Ayeshehshim, H.-C. Bandulet, R. Morandotti, J.-C. Kieffer, T. Ozaki, M. Reid, and F. A. Hegmann, "Nonlinear ultrafast modulation of the optical absorption of intense few-cycle terahertz pulses in *n*-doped semiconductors," *Phys. Rev. B* **79**, 193204 (2009).
14. P. T. Greenland, S. A. Lynch, A. F. G. van der Meer, B. N. Murdin, C. R. Pidgeon, B. Redlich, N. Q. Vinh, and G. Aeppli, "Coherent control of rydberg states in silicon," *Nature* **465**, 1057 – 1061 (2010).
15. M. Shalaby, C. Vicario, and C. P. Hauri, "Extreme nonlinear terahertz electro-optics in diamond for ultrafast pulse switching," *APL Photonics* **2**, 036106 (2017).
16. B. H. Kolner, R. A. Buckles, P. M. Conklin, and R. P. Scott, "Plasma characterization with terahertz pulses," *IEEE J. Sel. Top. Quantum Electron.* **14**, 505–512 (2008).
17. A. I. McIntosh, B. Yang, S. M. Goldup, M. Watkinson, and R. S. Donnan, "Terahertz spectroscopy: a powerful new tool for the chemical sciences?" *Chem. Soc. Rev.* **41**, 2072–2082 (2012).

18. B. Zhang, Z. Ma, J. Ma, X. Wu, C. Ouyang, D. Kong, T. Hong, X. Wang, P. Yang, L. Chen, and Y. Li, "1.4-mj high energy terahertz radiation from lithium niobates," arXiv: Opt. (2020).
19. S.-W. Huang, E. Granados, W. R. Huang, K.-H. Hong, L. E. Zapata, and F. X. Kärtner, "High conversion efficiency, high energy terahertz pulses by optical rectification in cryogenically cooled lithium niobate," *Opt. Lett.* **38**, 796–798 (2013).
20. J. A. Fülöp, Z. Ollmann, C. Lombosi, C. Skrobol, S. Klingebiel, L. Pálfalvi, F. Krausz, S. Karsch, and J. Hebling, "Efficient generation of thz pulses with 0.4 mj energy," *Opt. Express* **22**, 20155–20163 (2014).
21. F. Blanchard, X. Ropagnol, H. Hafez, H. Razavipour, M. Bolduc, R. Morandotti, T. Ozaki, and D. G. Cooke, "Effect of extreme pump pulse reshaping on intense terahertz emission in lithium niobate at multimillijoule pump energies," *Opt. Lett.* **39**, 4333–4336 (2014).
22. N. Horiuchi, "Ultrafast pulse switching," *Nat. Photonics* **11**, 331–331 (2017).
23. M. Shalaby, C. Vicario, and C. P. Hauri, "High-performing nonlinear visualization of terahertz radiation on a silicon charge-coupled device," *Nat. Commun.* **6**, 8439 (2015).
24. M. Shalaby and C. P. Hauri, "Demonstration of a low-frequency three-dimensional terahertz bullet with extreme brightness," *Nat. Commun.* **6**, 5976 (2015).
25. M. Shalaby, C. Vicario, K. Thirupugalmani, S. Brahadeeswaran, and C. P. Hauri, "Intense thz source based on bna organic crystal pumped at ti:sapphire wavelength," *Opt. Lett.* **41**, 1777–1780 (2016).
26. H. Zhao, Y. Tan, T. Wu, G. Steinfeld, Y. Zhang, C. Zhang, L. Zhang, and M. Shalaby, "Efficient broadband terahertz generation from organic crystal bna using near infrared pump," *Appl. Phys. Lett.* **114**, 241101 (2019).
27. A. Schneider, M. Neis, M. Stillhart, B. Ruiz, R. U. A. Khan, and P. Günter, "Generation of terahertz pulses through optical rectification in organic dast crystals: theory and experiment," *J. Opt. Soc. Am. B* **23**, 1822–1835 (2006).
28. K. Miyamoto, S. Ohno, M. Fujiwara, H. Minamide, H. Hashimoto, and H. Ito, "Optimized terahertz-wave generation using bna-dfg," *Opt. Express* **17**, 14832–14838 (2009).
29. M. Fujiwara, M. Maruyama, M. Sugisaki, H. Takahashi, S. ichiro Aoshima, R. J. Cogdell, and H. Hashimoto, "Determination of the d-tensor components of a single crystal of N-benzyl-2-methyl-4-nitroaniline," *Jpn. J. Appl. Phys.* **46**, 1528–1530 (2007).
30. J. Sun and S. Lucyszyn, "Extracting complex dielectric properties from reflection-transmission mode spectroscopy," *IEEE Access* **6**, 8302–8321 (2018).